Anisotropic elastic properties of human cortical bone tissue inferred from inverse homogenization and resonant ultrasound spectroscopy

Xiran Cai, Laura Peralta, Renald Brenner, Gianluca Iori, Didier Cassereau, Kay Raum, Pascal Laugier, Quentin Grimal

Anisotropic elastic properties of human cortical bone tissue inferred from inverse homogenization and resonant ultrasound spectroscopy

Xiran Cai[a,*], Laura Peralta[a], Renald Brenner[b], Gianluca Iori[c], Didier Cassereau[a], Kay Raum[c], Pascal Laugier[a], Quentin Grimal[a]

[a] *Sorbonne Université, INSERM UMR-S 1146, CNRS UMR 7371, Laboratoire d'Imagerie Biomédicale, 75006 Paris, France*
[b] *Sorbonne Université, CNRS UMR 7190, Institut Jean le Rond ∂'Alembert, 75005 Paris, France*
[c] *Berlin Brandenburg School of Regenerative Therapies, Charité-Universitätsmedizin Berlin, 13353 Berlin, Germany*

Abstract

Bone extravascular matrix (EVM) elasticity at several tens micrometer scale plays a key role in the mechanical behavior of bone at different length scales with implications on bone biology through mechanotransduction. The elastic properties of cortical bone EVM have been evaluated by several experimental methods, including nanoindentation, scanning acoustic microscopy (SAM) and mechanical testing on μm sized bone specimens. Nevertheless, these methods hardly give access to elastic anisotropy. In this work, we propose a novel inverse homogenization method to evaluate the anisotropic elastic properties of cortical bone EVM based on the transverse isotropic elastic tensor of millimeter-sized bone specimens measured by using resonant ultrasound spectroscopy and Fast Fourier Transform homogenization method. With the inverse homogenization method, the anisotropic EVM stiffness constants were evaluated on 50 human femoral cortical bone specimens from an elderly group. To our knowledge, this is the first time that the whole set of the EVM stiffness tensor is evaluated on the same specimen and on a large number of samples. Further comparison with the results from SAM and the degree of mineralization of bone (DMB) showed the potential of this method. Empirical laws between DMB and EVM anisotropic stiffness constants were also provided for the first time. With the anisotropic elasticity evaluated by the proposed method, more accurate models can be developed to better understand bone mechanics and biology, such as mechanotransduction.

Keywords: Bone extravascular matrix, Anisotropic stiffness, Inverse homogenization, Resonant ultrasound spectroscopy

1. Introduction

Bone size, shape and chemical composition have evolved to reach a compromise between mass, resistance to fracture and amplitude of elastic deformations [1]. The elastic properties of bone tissue at the millimeter scale (or mesoscale) [2], which play a key role in bone mechanics, depend on the properties and organization of the constituents at the nanoscale (mineral crystals and collagen molecules), at the micrometer scale (aligned mineralized collagen fibers forming lamellae) [3], and at the scale of a few tenth of microns where osteons and vascular pores are the main microarchitectural features.

*Corresponding author
Email address: xirancai@stanford.edu (Xiran Cai)

Bone tissue at the micrometer scale, i.e., the solid material in which vessels and nerves are embedded is often referred to as bone extravascular matrix (EVM), shortly bone matrix [4–6]. Bone material at the mesoscale is accordingly modelled as a network of vascular canals (Haversian and Volkman canals) embedded in a homogeneous bone matrix [7–9]. The elastic properties of EVM deserve a careful study because, combined with the micro-architecture of the vascular porosity, they determine bone elasticity at the mesoscale, which has a direct impact on the macroscopic mechanical behavior of whole bone. Also, for a given macroscopic loading, bone matrix elastic properties play a role in mechanotransduction as they govern the amplitude of matrix deformations which determine the interstitial fluid flow and the local strains sensed by osteocytes [10].

While, the inter-individual variations of EVM elastic properties in the general population are expected to be small [11, 12], considerable alteration of matrix elastic properties have been observed as a consequence of bone pathologies [13–15] and drugs [16, 17]. Several experimental approaches have been proposed to measure EVM elastic properties, which can be categorized as direct and indirect approaches. Direct approaches are nanoindentation [18, 19], scanning acoustic microscopy (SAM) [11, 20] and mechanical testing on μm-sized bone specimens [21–23]. For instance, using nano-indentation, elastic properties of trabecular and cortical bone tissues were found to be similar [24] and the interstitial tissue was found to be stiffer than osteonal tissue [25]. Using SAM, it was found that collagen fiber orientation has an impact on tissue elastic anisotropy probed at the microscale [26, 27].

These direct approaches have several limitations. Several assumptions on tissue elasticity (isotropy, assumed Poisson's ratio) are necessary to obtain the Young's modulus from a nanoindentation load-displacement curve [28]. Also, to get a representative value of bone matrix elasticity, several tens of indentation locations must be considered in the osteonal and interstitial tissues. SAM yields a map of the acoustic reflectivity of a bone surface using a high frequency ultrasound probe. Precisely, the method yields acoustic impedance values which can only be converted to Young's modulus using assumptions on tissue composition and Poisson's ratio [29]. Mechanical testing on μm-sized specimens requires dedicated experimental apparatus, long specimen's preparation time and it is not always possible to achieve a testing environment mimicking physiological conditions, e.g., as for experiments conducted in an electronic microscope [22].

An indirect approach to measure trabecular tissue elasticity was introduced by van Rietbergen et al. [30]; Tissue elasticity is retrieved by back-calculation combining experimental mechanical testing on a specimen of several millimeters and a corresponding micro-finite element model accounting for the specimen-specific trabecular microarchitecture. A linear relationship between tissue Young's modulus and bulk (measured) modulus can be assumed, which makes it possible to infer tissue modulus by searching for a good match between model and experimental data. A similar approach was proposed in which mechanical testing was replaced by ultrasound resonance testing [31].

Direct methods are designed to probe the EVM elastic modulus in one single direction (typically along the osteon axis), and inverse methods, as used to retrieve matrix elasticity in trabecular bone, assume isotropic

properties. This is a major limitation of both direct and indirect approaches: they hardly give access to elastic anisotropy unless very specific and elaborated techniques are implemented [19, 32]. However, EVM is not isotropic [25, 33, 34].

The present article introduces a novel indirect approach to retrieve the anisotropic EVM elastic properties. The new method is applied to a collection of human specimens to document the EVM elastic properties in an elderly population. Our approach, coined inverse homogenization, is similar to the back calculation procedure introduced by van Rietbergen et al. [30] for trabecular bone but it uses anisotropic elastic information at the mesoscale (experimental data) and the computation of a specimen's elastic tensor with homogenization. The method combines resonant ultrasound spectroscopy (RUS) which accurately measures the transverse isotropic elastic tensor of millimeter-sized bone specimens [35, 36] and Fast Fourier Transform (FFT) homogenization method [37, 38], which has been widely used in engineering material mechanics to evaluate the effective properties of composites and porous materials.

2. Materials and methods

2.1. Sample preparation

Bone specimens were harvested from the left femur of 29 human cadavers, provided by the Département Universitaire d'Anatomie Rockefeller (French body donation to science program, declaration number: DC-2015–2357; Laboratory of Anatomy, Faculty of Medicine Lyon Est, University of Lyon, France) through the French program on voluntary corpse donation to science. Among the donors, 16 were females and 13 were males ($50-95$ years old, 77.8 ± 11.4, mean $\pm$ SD). The nominal specimen size was $3 \times 4 \times 5$ mm^3 in radial (axis 1), circumferential (axis 2) and axial directions (axis 3), respectively, defined by the anatomical shape of the femoral diaphysis. Details of sample preparation can be found in Cai et al. [39].

2.2. Bulk elasticity of the bone specimens

Cortical bone was assumed to be a transversely isotropic material [40, 41]; using Voigt notation, the matrix form of the stiffness tensor writes

$$\mathbf{C} = \begin{pmatrix} C_{11} & C_{12} & C_{13} & 0 & 0 & 0 \\ C_{12} & C_{11} & C_{13} & 0 & 0 & 0 \\ C_{13} & C_{13} & C_{33} & 0 & 0 & 0 \\ 0 & 0 & 0 & C_{44} & 0 & 0 \\ 0 & 0 & 0 & 0 & C_{44} & 0 \\ 0 & 0 & 0 & 0 & 0 & C_{66} \end{pmatrix}, \tag{1}$$

where, $C_{12} = C_{11} - 2C_{66}$ and $(1-2)$ is the isotropy plane; C_{11} and C_{33} are the longitudinal stiffness constants, C_{12} and C_{13} are the off-diagonal stiffness constants; and C_{44} and C_{66} are the shear stiffness constants.

In the present study, we use already published anisotropic elasticity data of cortical bone specimens measured with RUS [39]. The main sources of experimental errors are related to the irregularities of specimen's geometry and the uncertainties on the values of extracted resonant frequencies. These errors have been documented in a previous study and are of the order of 1.7% for shear stiffness constants, 3.1% for longitudinal and off-diagonal stiffness constants [42]. Hereafter, the stiffness constants measured by RUS are referred to as C_{ij}^{EXP}.

2.3. Bone microstructure and degree of mineralization

Degree of mineralization of bone (DMB) and vascular porosity (ϕ) data used in this work has been published and was obtained following the imaging protocol described in detail in Cai et al. [39]. Briefly, specimens were imaged with a pixel size of 6.5 μm with synchrotron radiation micro-computed tomography (SR-μCT) at the European Synchrotron Radiation Facility (ESRF) using a SR-μCT setup based on a 3-D parallel beam geometry acquisition [43, 44]. The calibrated gray levels of each specimen were converted into volumetric DMB as detailed in Nuzzo et al. [45].

For the purpose of homogenization (see Section 2.5), the 3D volume of each specimen was slightly rotated using Fiji [46] so that the image reference frame coincides with the orientation of the specimen's faces. In each specimen, the largest possible rectangular parallelepiped volume of interest (VOI) was selected manually to achieve the largest available volume (average size about $2.8 \times 3.9 \times 4.8$ mm^3). The VOIs were binarized by simple thresholding treating the void volumes as a solid and the bone phase as a background, from which ϕ of each specimen was measured. Finally, the voxel size was downsampled to 35 μm after having conducted convergence tests reported in Appendix B. The average total number of voxels in each VOI was about 1.2 million.

2.4. Bone matrix acoustic impedance

A subset of 23 specimens (all from the lateral quadrant) were measured with a custom SAM to provide an independent measurement of tissue elastic properties for comparison with the results of inverse homogenization. The SAM operating with a spherically focused 100-MHz transducer (KSI 100/60°, Krämer Scientic Instruments, Herborn, Germany) was used to probe the acoustic impedance normal to the samples surfaces according to the measurement procedure extensively detailed in [47]. Calibrated impedance (Z) maps were obtained with a lateral resolution of 19.8 μm for the faces perpendicular to radial and axial directions. The Z-maps were segmented allowing the separation of vascular porosity and bone EVM. The acoustic impedance of the matrix was determined from the segmented maps of the specimens. The small pores (Volkmann's canal, osteocyte lacunae) could not be resolved so that they contributed to the probed bulk matrix properties.

Matrix impedance in the probing direction, denoted $Z_i (i = 1, 3)$, was defined as the mean value of the Z-map scanned in the face of direction i. Matrix impedance was then converted to EVM stiffness using the following equation:

$$C_{ii}^{Z} = \frac{Z_i}{\rho_t}, \tag{2}$$

where $\rho_t = 1.12 + 0.73 \cdot \mathrm{DMB} - 0.033 \cdot \mathrm{DMB}^2$ is the tissue density converted from DMB values [48].

2.5. Forward problem: homogenization to simulate bulk stiffness

Each specimen's VOI was considered as a representative volume for homogenization containing two homogeneous phases: vascular porosity and EVM. The elastic properties of the pore voxels were defined with a bulk modulus of 2.2 GPa and a null shear modulus, corresponding to elastic properties of water. The EVM voxels were allocated transverse isotropic elastic properties C_{ij}^m. The isotropy plane of the EVM material was taken to be the plane $1-2$. The terms C_{ij}^m are the unknowns of the inverse homogenization problem.

The bulk stiffness tensor C_{ij}^{FFT} of each VOI was evaluated by the FFT homogenization method [37, 38]. Briefly, the bulk stiffness tensor is obtained after solving the local mechanical problem in the VOI (V) consisting of the equilibrium equation, generalized Hooke's law as constitutive equation, compatibility of the displacement field and boundary conditions. The phases are assumed to be perfectly bonded. The local problem closed by periodic boundary conditions [49, 50] can be solved by the FFT-based numerical approach proposed by Moulinec and Suquet [37].

The implementation of the method has been described in [9]. Note that no elastic symmetry assumption was made for the calculation of the effective stiffness tensor. For the requirements of the present study, we implemented a parallelized version of the FFT method. One loading in the FFT homogenization method took around 50 iterations in our specimens and the effective stiffness tensor could be computed in about 1 minute on a workstation (CPU, Intel Xeon E5-2695 v3, 8 threads per loading).

For all VOIs, the values of the off-diagonal terms of the homogenized stiffness tensor C^{FFT}, which are null in the case of orthotropy when the tensor is expressed in the material basis, were at least two orders of magnitude smaller than the other terms. These off-diagonal terms were, therefore, disregarded, i.e., the 12 coefficients with index $kl = 11, 22, 33, 44, 55, 66, 12, 21, 13, 31, 23, 32$ were kept.

2.6. Inverse homogenization to recover EVM stiffness

The inverse homogenization consists in determining the matrix stiffness tensor $\mathbf{C^m}$ which provides an optimum match between $\mathbf{C^{EXP}}$ and $\mathbf{C^{FFT}}(\mathbf{C^m})$ Two approaches have been implemented: (1) The 'calibration approach' assumes that one mesoscale coefficient C_{ij}^{FFT} is fully determined by the porous microstructure and its EVM counterpart C_{ij}^m. (2) The 'optimization approach' determines the EVM stiffness constants without such assumption, i.e., it accounts for the possible dependence of one term of the mesoscale tensor C_{ij}^{FFT} on all EVM stiffness constants. The 'calibration approach' is straightforward and less demanding in terms of computational resources, but intrinsically less precise to determine C_{ij}^m. We found that the two approaches lead to only slightly different results. Only the details and the results of the 'optimization approach' are detailed in the paper. The methodology and results of the 'calibration approach' are reported in Appendix A.

EVM stiffness constants $\mathbf{C}^m$ of each specimen were obtained by minimizing the objective function defined as the root-mean-square-error (RMSE) between experimental and homogenized bulk stiffness constants. That is, for each specimen, we solve

$$RMSE(\mathbf{C}^m) = \sqrt{\frac{1}{12}\sum_{kl}\left(\frac{C_{kl}^{EXP} - C_{kl}^{FFT}(\mathbf{C}^m)}{C_{kl}^{EXP}}\right)^2} \times 100\%, \tag{3}$$

Note that the 12 non-zero coefficients (labeled by $_{kl}$) are used in eq. 3. The Nelder-Mead Simplex Method implemented in Matlab Optimization Toolbox Release 2017b (MathWorks, Natick, MA), which does not require derivative information, was used to solve the minimization problem. The iterative solver stopped when, for two consecutive iterations, both the difference of the objective function values (eq. 3), and the difference of the norms of C_{ij}^m, were smaller than 0.001. For most of the specimens, the optimization stopped after about 130 iterations which costed about 130 minutes per specimen. The optimization procedure was initialized at the values ($\mathbf{C}^{m0}$) of $C_{11}^{m0} = 24.4$ GPa, $C_{33}^{m0} = 33.5$ GPa, $C_{13}^{m0} = 14.7$ GPa, $C_{44}^{m0} = 6.9$ GPa, $C_{66}^{m0} = 5.4$ GPa. These values, reported in [9], were found by minimizing the differences between experimental and homogenized stiffness constants for the entire collection of specimens.

2.7. Estimation of the precision of inverse homogenization to recover EVM stiffness

$\mathbf{C}^m$ is recovered from experimental elasticity data and the images of each specimen's microstructure. The images have a high contrast and a high resolution so that there is little concern about the precision of the reconstruction of the pore vascular network. The method of solution used for the forward problem yields the exact solution of the continuum mechanics problem with a controlled numerical precision. It follows that the uncertainties on C_{ij}^m mostly stem from the experimental uncertainties on C_{ij}^{EXP}. We conducted an error propagation analysis using Monte-Carlo (MC) simulations to estimate the errors on C_{ij}^m due to the uncertainties on C_{ij}^{EXP}.

Three specimens with porosities covering the entire porosity range (5.0%, 9.9% and 15.4%) were selected for the MC simulations to account for an expected dependence of the error on porosity. The experimental uncertainties on stiffness constants were modeled with independent normal distributions. The distributions were centred at mesoscale stiffness values obtained from the FFT homogenization of each of the three specimen's VOI with EVM stiffness $\mathbf{C}^{m0}$. The width of the distributions were consistent with the typical experimental uncertainties for longitudinal and off-diagonal stiffness constants (SD of 3.0%) and shear stiffness constants (SD of 1.5%). A set of 1000 independent realizations of mesoscale stiffness tensors were drawn from the normal distributions. The EVM stiffness C_{ij}^m was calculated for each realization of mesoscale stiffness tensor using inverse homogenization and compared with $\mathbf{C}^{m0}$ to calculate the relative error on each coefficient, defined as

$$\delta C_{ij}^m = (C_{ij}^m - C_{ij}^{m0})/C_{ij}^{m0} \times 100\%, \tag{4}$$

2.8. Data analysis

Linear least squares regressions were conducted to analyze the relationships between elastic properties, impedance and DMB. Pearson's correlation coefficient are reported. Normality of the distributions of the C_{ii}^m and C_{ii}^Z was verified using the ShapiroWilk test. Paired t-test was used to test if C_{ii}^m and C_{ii}^Z were different. The level of significance for all the tests was set to $p = 0.05$.

3. Results

3.1. Descriptive statistics

The specimens of one subject with a porosity higher than 30% was not included in the analysis. Another specimen was broken during sample preparation. Finally 55 specimens were used for this study.

The bulk elasticity of five specimens with a porosity larger than 14.5% were found to be slightly orthothropic due to the shape of the pore network [9]. Precisely, the relative difference between C_{22}^{FFT} and C_{11}^{FFT}, or between C_{44}^{FFT} and C_{55}^{FFT} exceeded 3% for these five specimens. This violates the assumption of a transverse isotropic material used to process RUS measurements. Despite the fact that, for these specimens, the inverse homogenization optimization lead to a relatively good fit with a RMSE (eq. 3) between 1 and 2%, these specimens were discarded. The results presented below are consequently given for 50 specimens.

Experimental stiffness constants, porosity, DMB and matrix impedance are summarized in Table 1. The coefficient of variation (CV) of DMB was about 2% which is smaller than the CV of Z_i $(4.2 - 4.3\%)$ and C_{ij}^{EXP} $(7 - 14\%)$.

Table 1: The average, SD and range of the experimental data of the stiffness constants (C_{ij}^{EXP}), porosity (ϕ), DMB (ρ_m) and matrix acoustic impedance (Z_i). Note that Z_i was measured on 23 specimens from the lateral quadrant.

	C_{11}^{EXP} (GPa)	C_{33}^{EXP} (GPa)	C_{13}^{EXP} (GPa)	C_{44}^{EXP} (GPa)	C_{66}^{EXP} (GPa)
Mean±SD	20.1 ± 1.5	29.5 ± 1.3	12.0 ± 0.9	6.0 ± 0.4	4.5 ± 0.5
Range	$16.9 - 23.8$	$25.7 - 32.1$	$9.3 - 14.1$	$4.7 - 6.9$	$3.5 - 5.9$
	ϕ (%)	ρ_m (g/cm^3)	Z_1 (Mrayl)	Z_3 (Mrayl)	
Mean±SD	6.5 ± 2.6	1.02 ± 0.02	6.8 ± 0.3	7.4 ± 0.3	
Range	$1.8 - 12.1$	$0.95 - 1.06$	$6.2 - 7.5$	$6.9 - 8.1$	

The RMSEs after inversion (eq. 3) were small, between $0.06 - 1.01\%$ (Mean $\pm$ SD $= 0.26 \pm 0.19\%$). The EVM stiffness constants C_{ij}^m and the engineering moduli (obtained by inverting the stiffness tensor) are summarized in Table 2. The CVs of C_{ij}^m $(3.0 - 7.1\%$, Table 2), EVM Young's moduli $(4.5 - 5.5\%)$ and EVM Poisson's ratios $(5.3 - 11.5\%)$ were greater than that of ρ_m (2%, Table 1).

3.2. Error propagation analysis

The distribution of each δC_{ij}^m (eq. 4) was found to be normally distributed (Shapiro-Wilk's test). The results are summarized in Table 3. The offset (bias) of δC_{ij}^m from zero was small, less than 0.8%. The

Table 2: The mean, SD and range of the EVM stiffness constants C_{ij}^m and engineering moduli.

	C_{11}^m (GPa)	C_{33}^m (GPa)	C_{13}^m (GPa)	C_{44}^m (GPa)	C_{66}^m (GPa)
Mean±SD	24.5 ± 1.2	33.6 ± 1.1	14.7 ± 1.0	7.0 ± 0.3	5.4 ± 0.4
Range	$21.7 - 27.5$	$31.4 - 36.2$	$12.1 - 16.7$	$6.1 - 7.5$	$4.5 - 6.3$
	E_1^m (GPa)	E_3^m (GPa)	ν_{23}^m	ν_{31}^m	ν_{12}^m
Mean±SD	15.1 ± 0.8	22.4 ± 1.0	0.26 ± 0.02	0.38 ± 0.02	0.41 ± 0.03
Range	$13.2 - 17.0$	$20.3 - 24.9$	$0.19 - 0.31$	$0.34 - 0.41$	$0.32 - 0.48$

uncertainty characterized by SDs of δC_{ij}^m were between $3.1-4.7\%$ for longitudinal and off-diagonal coefficients and $1.5-1.9\%$ for shear coefficients (Table 3). These uncertainties are comparable with the SDs of the errors modeled in MC simulations and corresponding to experimental uncertainty on C_{ij}^{EXP}. We noted that the SD of δC_{ij}^m increases as porosity increases.

Table 3: The errors (Mean±SD in %) on EVM stiffness constants affected by the experimental errors on the bulk stiffness constants. Calculation were performed for 3 specimens of 5.0%, 9.9% and 15.4% porosity.

	$\phi = 5.0\%$	$\phi = 9.9\%$	$\phi = 15.4\%$
δC_{11}^m	0.21 ± 3.49	-0.01 ± 3.96	-0.76 ± 4.66
δC_{33}^m	0.02 ± 3.05	-0.09 ± 3.06	-0.17 ± 2.99
δC_{13}^m	0.17 ± 3.12	0.03 ± 3.55	-0.35 ± 3.90
δC_{44}^m	-0.12 ± 1.49	-0.07 ± 1.58	0.08 ± 1.59
δC_{66}^m	-0.16 ± 1.62	0.07 ± 1.70	0.69 ± 1.87

3.3. Comparison between EVM stiffness derived by RUS and SAM

SAM provides a direct assessment of acoustic impedance Z which is a good proxy for stiffness. Impedance can be converted to stiffness C_{ii}^Z according to eq. 2 which can be directly compared to C_{ii}^m. EVM longitudinal stiffness constants evaluated by inverse homogenization and SAM are compared in Table 4. The values of C_{ii}^m and C_{ii}^Z were significantly different ($p < 0.002$). The mean value of C_{11}^m was about 5.1% smaller than that of C_{11}^Z, while the mean value of C_{33}^m was about 10.2% greater than that of C_{33}^Z. C_{ii}^Z exhibited a greater variability (CV was about 8%) compared to C_{ii}^m (CV between $3-5\%$). No significant correlation was found between C_{11}^m and C_{11}^Z, nor between C_{33}^m and C_{33}^Z.

Table 4: Comparison between EVM stiffness measured by RUS and SAM.

	Mean±SD	Range
C_{11}^m (GPa)	24.0 ± 1.2	$21.7 - 26.7$
C_{11}^Z (GPa)	25.4 ± 2.0	$21.5 - 30.6$
C_{33}^m (GPa)	33.5 ± 1.1	$31.4 - 36.2$
C_{33}^Z (GPa)	30.4 ± 2.4	$25.8 - 35.3$

Figure 1 and 2 summarize the relationships observed between C_{ij}^m and Z_i. The CV of C_{ij}^m $(3.0 - 7.1\%)$ is comparable with that of Z_i. Significant positive correlations were observed between Z_1 and the C_{44}^m, C_{66}^m $(0.52 < r < 0.60$, Figure 1), and between Z_3 and C_{44}^m $(r = 0.42$, Figure 2). Trends of positive (not significant) correlations were also observed between Z_1 and C_{11}^m, C_{33}^m and C_{13}^m $(0.34 < r < 0.38$, Figure 1), and between Z_3 and C_{66}^m $(r = 0.36$, Figure 2).

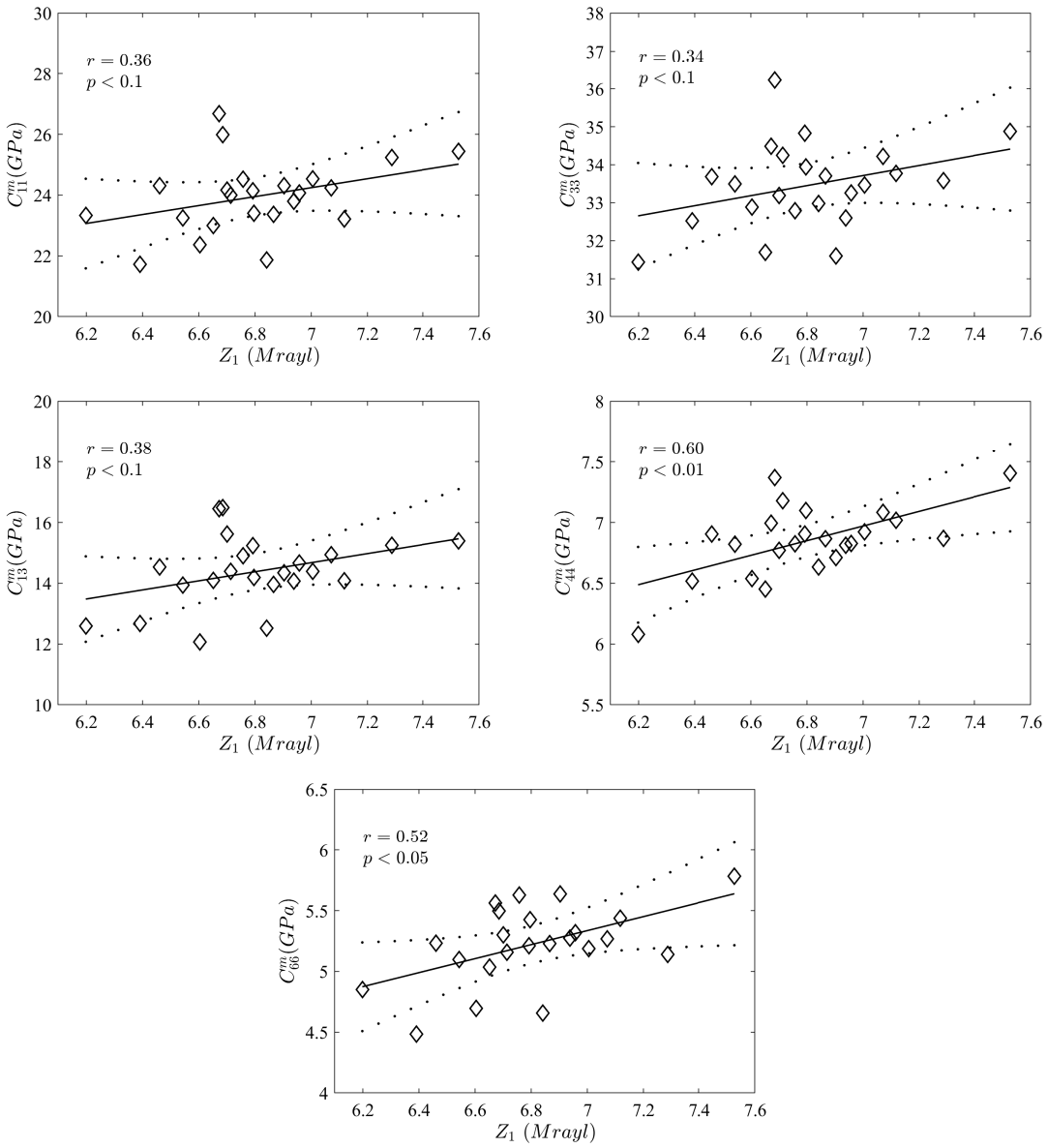

Figure 1: Relationships between Z_1 and C_{ij}^m, and the corresponding linear regression model (solid line) with the 95% CI (dot line). r is the Pearson's correlation coefficient.

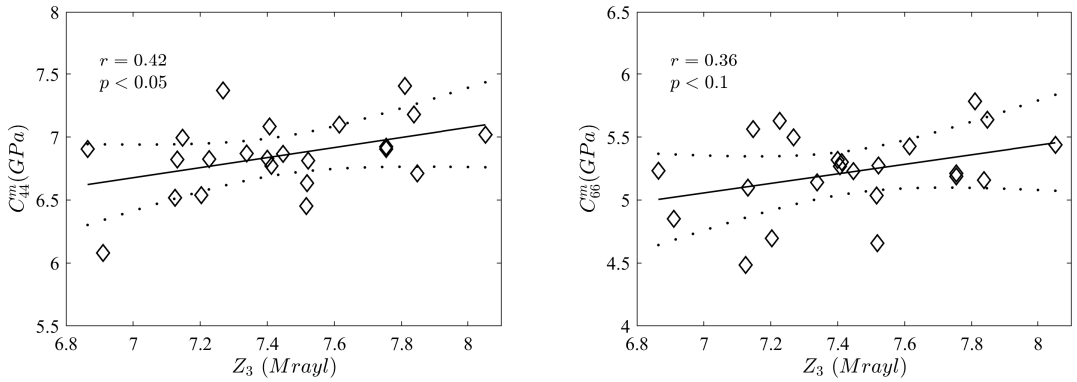

Figure 2: Relationships between Z_3 and C^m_{44}, C^m_{66}, and the corresponding linear regression model (solid line) with the 95% CI (dot line). r is the Pearson's correlation coefficient.

3.4. Variations of EVM stiffness with DMB

Significant correlations were observed between ρ_m and C^m_{44}, C^m_{66} ($0.65 < r < 0.70$, Figure 3). The data suggest a positive relationship might exist between C^m_{11}, C^m_{33}, C^m_{13} and ρ_m, but the correlations ($0.24 < r < 0.27$) were not significant. Also, ρ_m positively correlated with E^m_1, ν^m_{23} and ν^m_{31} ($0.32 < r < 0.59$), and negatively with ν^m_{12} ($r = -0.61$) (Figure 4). The linear regression equations between ρ_m and EVM stiffness constants are given in Table 5.

Table 5: Empirical laws between ρ_m and C^m_{ij}.

	Laws
C^m_{11}	$14.96 \times \rho_m + 9.28$
C^m_{33}	$13.99 \times \rho_m + 19.39$
C^m_{13}	$11.79 \times \rho_m + 2.69$
C^m_{44}	$8.82 \times \rho_m - 2.02$
C^m_{66}	$11.13 \times \rho_m - 5.97$

4. Discussion

In this work, we introduced an inverse homogenization approach to evaluate the anisotropic elastic properties C^m_{ij} of cortical bone EVM. The approach uses a measurement of the transverse isotropic stiffness tensor at the mesoscale (with RUS) and assumes that the EVM is itself transverse isotropic. The EVM stiffness values obtained are to be understood as 'mean' values representative of the entire volume of the specimen as the forward problem (homogenization) assumes a homogeneous EVM throughout the specimen's volume. One key aspect of the work is that the homogenization is performed with the real vascular pore structure obtained with the state-of-the-art 3D μ-CT imaging. Also, the VOI used as a representative volume element for homogenization almost matches the specimen volume assessed by RUS, enabling a direct

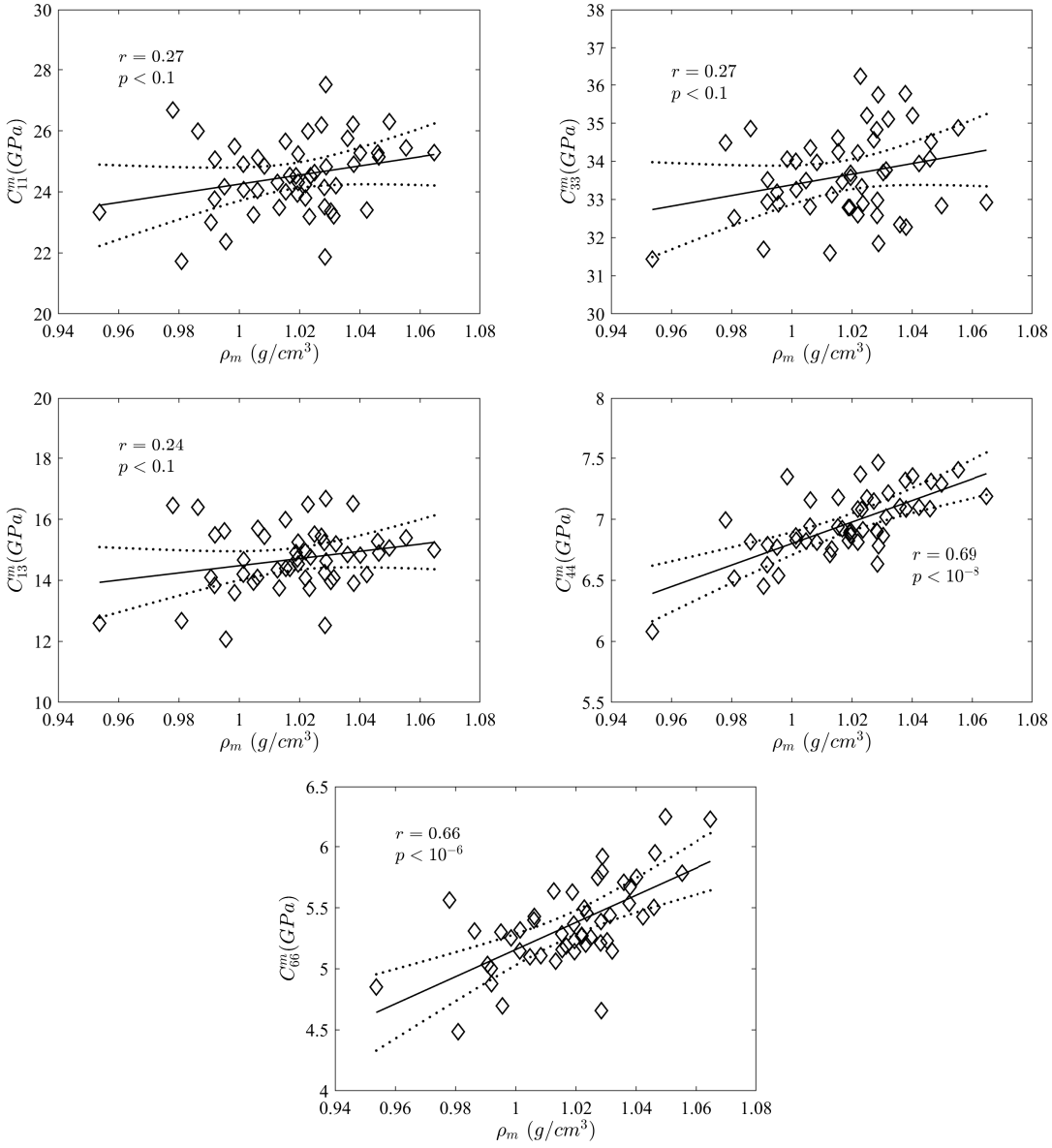

Figure 3: Relationships between ρ_m and C_{ij}^m, and the corresponding linear regression model (solid line) with the 95% CI (dot line). r is the Pearson's correlation coefficient.

comparison between predicted and measured mesocale stiffness. It is noteworthy that the method provides the complete elastic tensor, from which the engineering moduli (i.e., Young's moduli, shear moduli and Poisson's ratios) can be obtained.

The fine knowledge of experimental errors on the stiffness constants measured by RUS [42] allows performing a realistic estimation of the errors on C_{ij}^m determined by inverse homogenization. The magnitude of the errors (SD$= 1.5 - 1.9\%$ for shear coefficients and SD $= 3.1 - 4.7\%$ for longitudinal and off-diagonal coefficients, Table 3) were close to the errors on the bulk stiffness constants measured with RUS. Note that the errors on C_{11}^m were a bit larger than on C_{33}^m, which may be explained by the fact that small anisotropy in

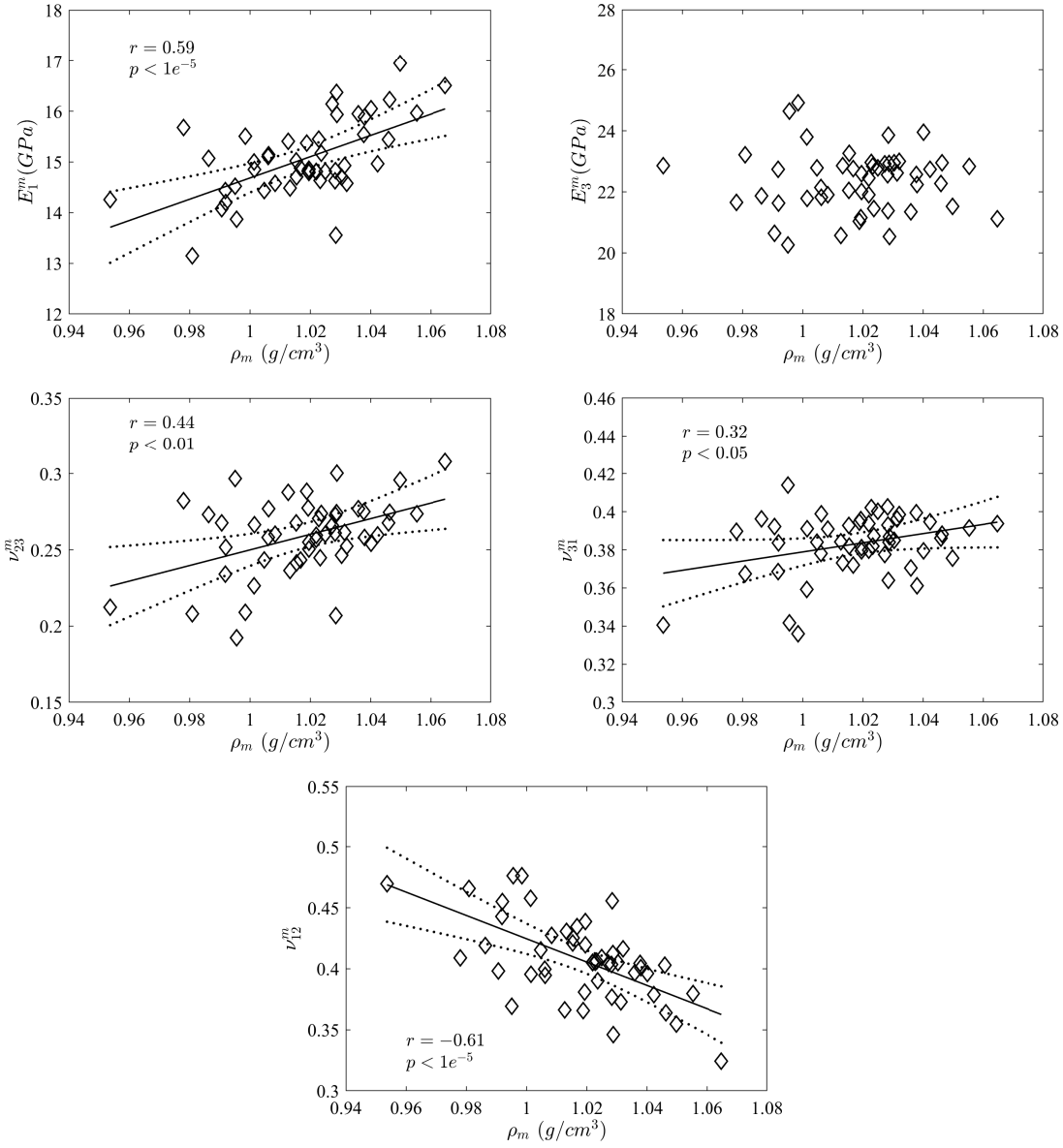

Figure 4: Relationships between ρ_m and EVM Young's moduli and Poisson's ratio, and the corresponding linear regression model (solid line) with the 95% CI (dot line). r is the Pearson's correlation coefficient.

the transverse plane is disregarded in the inverse homogenization process, forcing an 'artificial' adjustment of C_{11}^m. The errors on the EVM stiffness may be minimized by improving the precision and accuracy of RUS [42].

The average values of EVM stiffness constants and Young's moduli agreed well with the values reported in previous studies measured on human femoral bone as well [19, 24, 32] (Table 6). These values from the literature were evaluated by various approaches, including acoustic, indentation and micromechanical model-based methods. Specifically, the average values of C_{33}^m, C_{44}^m, C_{66}^m and all the engineering moduli fell inside the range of values measured by SAM and nano-indentation. For C_{11}^m and the two off-diagonal

coefficients C_{13}^m and C_{12}^m, our values were a bit higher. As far as we are aware, only two articles reported the measurement of the entire anisotropic elastic tensor of the EVM [19, 32]. The method used by Lakshmanan et al. [32], based on SAM measurements relies on empirical laws (relating acoustic impedance to several stiffness constants) and idealized micromechanical models (for the off-diagonal coefficients) to retrieve the elastic tensor. The method used by Franzoso and Zysset [19], based on nano-indentation measurements, uses an indenter shape-dependent model [51] and a fabric tensor incorporating important assumptions (fibers organization and simplified intrinsic material model).

For instance, our data and the data from [32] respect the inequality relation $\nu_{23} < \nu_{31} < \nu_{12}$ noted in Cowin [52], while not the data from Franzoso and Zysset [19]. In our approach, we only assume transverse isotropic elastic symmetry for EVM. Furthermore, we provide data for a relatively large number of subjects.

Table 6: Comparison between the bone EVM elastic properties found in this work and in previous studies. The values are summarized as mean ± SD except those converted by the mean values of the coefficients (elastic tensor to Engineering moduli or conversely). Franzoso: Franzoso and Zysset [19]; Lakshmanan: Lakshmanan et al. [32]; Turner: [24].

	Acoustic			Nano-indentation	
	This study	Lakshmanan	Turner		Franzoso
C_{11}^m (GPa)	24.5 ± 1.2	21.9 ± 2.1	22.4 ± 0.8	—	14.3
C_{33}^m (GPa)	33.6 ± 1.1	29.9 ± 5.0	28.3 ± 0.3	—	38.6
C_{13}^m (GPa)	14.7 ± 1.0	9.7 ± 1.6	—	—	12.3
C_{12}^m (GPa)	13.8 ± 0.9	9.2 ± 1.5	—	—	10.3
C_{44}^m (GPa)	7.0 ± 0.3	6.7 ± 1.2	—	—	7.7 ± 0.5
C_{66}^m (GPa)	5.4 ± 0.4	6.4	—	—	4.7 ± 0.4
E_1^m (GPa)	15.1 ± 0.8	16.8	14.9 ± 0.5	16.6 ± 0.3	9.2 ± 0.6
E_3^m (GPa)	22.4 ± 1.0	23.8	20.6 ± 0.2	23.5 ± 0.2	24.7 ± 2.7
ν_{23}^m	0.26 ± 0.02	0.22	—	—	0.29 ± 0.02
ν_{31}^m	0.38 ± 0.02	0.31	—	—	0.56 ± 0.02
ν_{12}^m	0.41 ± 0.03	0.32	—	—	0.25 ± 0.01

SAM provided impedance data and combined with a model to derive mass density from DMB, provided an independent measure of EVM stiffness. SAM is seemingly the most appropriate technique to perform a comparison with our EVM stiffness values because it scans entire surfaces of the cuboid specimens; SAM data can then be averages, yielding values directly comparable with C_{ij}^m derived from inverse homogenization. We found significant correlations between impedance data and EVM shear stiffness (Figure 1) and 2). For the other stiffness constants, the data suggest a relationship might exist with acoustic impedance but no significant correlations were observed. The differences between the mean values of the longitudinal EVM stiffness evaluated by inverse homogenization and derived from SAM were relatively small ($< 10.2\%$, Table 4) considering that the two methodologies are different. However, stiffness derived with SAM and inverse homogenization were not correlated. The low and non-significant correlation may in part be due to the fact that only 23 among 55 specimens were measured with SAM.

The reason for the lack of correlation is likely due to experimental errors of both techniques. RUS is intrinsically more accurate for shear stiffness compared to longitudinal stiffness [53, 54], which would explain that correlations are found between impedance and shear stiffness. Note that, SAM requires a flat and polished surface to measure the acoustic impedance. This is obtained by a manual polishing of the specimens which is especially difficult to realize when the sample size is small, as is the case for our specimens (Z_1 and Z_3 were measured on the 4×5 mm^2 and 3×4 mm^2 surfaces, respectively). In addition, SAM is a surface measurement, whereas the C_{ij}^m evaluated by inverse homogenization are representative of the entire volume of a specimen. The relatively narrow range of variation of the EVM stiffness, combined with measurement errors are likely to weaken correlations.

Significant correlations between DMB (averaged in the specimen's volume) and EVM shear stiffness (Figure 3), and most of the EVM engineering moduli (Figure 4) were observed, which has not been reported before. Similar to the observation for impedance data, the correlation between DMB and the EVM longitudinal stiffness were not significant. This is consistent with the magnitude of the errors in stiffness measured by RUS as previously mentioned. Furthermore, opposite correlations between DMB and the Poisson's ratios were observed suggesting different deformation behavior in different directions may exist at the tissue level as bone is mineralizing, which may be interesting to investigate in the future. Note that the repeatability of the DMB measured by SR-μCT varying beam energy was reported to be as small as 0.26% using the same setup on beamline ID 19 at ESRF [55], which may be a reason why correlations with stiffness are found although the range of variation of DMB is small.

The bone specimens used in this study are from donors with undocumented medical history. Overall, the presented EVM stiffness data set (Table 2) may only represent a group of elderly population without a specific bone pathology. As expected for such a population, the EVM stiffness values vary in a relatively small range (from 4.8% to 15.4%). This data may be used as a reference data set to compare with EVM stiffness in bone pathology.

Some limitations in this study should be mentioned. Although the entire EVM stiffness tensor of the specimens is provided in this work, the accuracy of the values need further investigation. The comparison with SAM-derived stiffness shows a relatively good agreement, and the comparison with the values obtained from nanoindentation indicates that the values of EVM stiffness obtained with inverse homogenization are in the expected range. Most importantly, the correlations between some stiffness constants and DMB demonstrate that the proposed method is sufficiently precise to probe small differences of elasticity due to small changes of DMB.

We assumed that the EVM is homogeneous. In reality, bone matrix mechanical properties are heterogeneous depending on the local variations of the degree of mineralization (differences of elastic modulus between osteonal and interstitial region in cortical bone[25, 56]) and microfibril orientation [26]. Though it has been shown in trabecular bone that the bulk elastic properties only changed about 2% considering an heterogeneous model [57], the effect of neglecting tissue heterogeneity has not been quantified in cortical

bone.

We also assumed that the EVM stiffness is transverse isotropic. This was a necessary assumption because the RUS experimental data itself was obtained with this assumption at the mesoscale level. This assumption proved to be valid for most of the specimens, however it may not be valid for specimens taken at other anatomical sites.

5. Conclusion

To conclude, we introduced an inverse homogenization method to evaluate cortical bone EVM anisotropic elastic properties. Our approach provides the entire EVM stiffness tensor with a precision of a few percent. The EVM stiffness tensor is provided for 50 specimens from 26 elderly donors exhibiting the range of variation for this population. The present work is unprecedented documentation of EVM anisotropic elasticity. One important perspective is the quantification of *in situ* strains of the EVM under loading which has consequences for the mechanotransduction process.

Acknowledgment

This work has received financial support from the Agency National Research under the ANR-13-BS09-0006 MULTIPS project. The authors would like to thank ESRF for the access of beamline at ID 19 and 17 and the help from Cécile Olivier and Françoise Peyrin for performing SR-μCT experiments.

Appendix A. Calibration approach

From several preliminary tests, we found that the coupling between C_{ij}^{FFT} and its counterpart C_{ij}^{m} (e.g., between C_{11}^{FFT} and C_{11}^{m}) is much stronger than the other EVM stiffness constants which means that specimen-specific relationships can be built between them. Specifically, the relationship between C_{11}^{FFT} (as an example) and C_{11}^{m} was established by varying the values of C_{11}^{m} starting from C_{11}^{m0} while fixing C_{33}^{m0}, C_{13}^{m0}, C_{44}^{m0}, C_{66}^{m0} (see Figure A.1). The range of variations were $C_{11}^{m0} \pm 10$ GPa, $C_{33}^{m0} \pm 12$ GPa, $C_{13}^{m0} \pm 6$ GPa, $C_{44}^{m0} \pm 4$ GPa and $C_{66}^{m0} \pm 3$ GPa (5 evenly distributed points in the interval for each coefficient), respectively. Then, the C_{11}^{EXP} was projected to C_{11}^{m} given the established relationship (Figure A.1). It costed about 30 minutes ($5 \times 6 = 30$ forward computations) to calculate EVM stiffness constants of a specimen in the calibration approach.

The RMSE (eq. 3) was also calculated for each specimen after $\mathbf{C}^m$ was obtained to compare with the ones from optimization approach. The RMSEs from the calibration approach were between $0.12 - 2.52\%$ (Mean $\pm$ SD $= 0.76 \pm 0.46\%$) greater than that from the optimization approach in general which is expected. The optimization approach takes all the coupling between the coefficients into account, i.e., it allows more degrees of freedom. Therefore, it is expected that the optimization approach would produce smaller RMSEs.

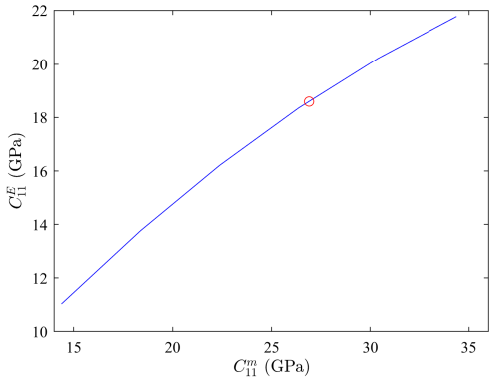

Figure A.1: An example of a specimen-specific relationship (solid curve) between C_{11}^{FFT} and C_{11}^{m}. The latter was projected (circle) by C_{11}^{EXP} using the relationship.

Bland-Altman's plots between the C_{ij}^{m} from the two approaches showed that only a small bias existed for C_{11}^{m} (0.15 GPa), but not for the other coefficients (< 0.07 GPa) and the relative differences are quite small (CV was between $0.35 - 0.96\%$) compared to experimental errors. Therefore, one can conclude that there is no significant difference between the two inverse homogenization approaches.

Appendix B. Convergence study

The convergence study was carried out on the three specimens mentioned in Section 2.7 whose original pixel size (ps) of the 3D images was 6.5 μm.

Appendix B.1. Forward problem

The convergence study for the forward problem was mainly used to determine the pixel size for the VOIs. Details can be found in Cai et al. [9] (Appendix B.2.).

Appendix B.2. Inverse problem

The ps of the images of each specimen was increased to 10, 15, 20, 25, 30 and 35 μm, respectively, in order to study how the image resolution affects the result of the inverse homogenization. The bulk stiffness constants of each specimen, calculated by the FFT homogenization when $ps = 10$ μm and using C_{ij}^{m0} as the EVM stiffness constants, were used as the input. Applying the inverse homogenization on the images at the other ps ($15 - 35$ μm) for each specimen, the bias between EVM stiffness constants $C_{ij}^{m,ps}$ evaluated at different ps and C_{ij}^{m0} was quantified by the RMSE denoted below:

$$RMSE(ps) = \sqrt{\frac{1}{5}\sum_{ij}\left(\frac{C_{ij}^{m,ps} - C_{ij}^{m0}}{C_{ij}^{m0}}\right)^2} \times 100\% \tag{B.1}$$

Results showed that when $ps \leqslant 35$ μm, all the RMSEs were less than 0.5%. Compared with the experimental errors in RUS, these values are smaller. To this end, $ps = 35$ μm was considered as an appropriate value for the 3D images of the specimens and was chosen in this work.

Appendix C. Validation of the inversion

The effective stiffness constants C_{ij}^{FFT0} of all the 55 specimens were calculated by the FFT homogenization with the values C_{ij}^{m0} for bone EVM and the pixel size of the images was 35 μm. Using C_{ij}^{FFT0} as the input, both the calibration and optimization approaches were implemented to calculate the EVM stiffness constants C_{ij}^{m} and the RMSE of each specimen was evaluated as:

$$RMSE = \sqrt{\frac{1}{5}\sum_{ij}\left(\frac{C_{ij}^{m} - C_{ij}^{m0}}{C_{ij}^{m0}}\right)^2} \times 100\% \tag{C.1}$$

The results are depicted in Figure C.2 in which we observed that all the RMSE are less than 0.15% and 0.018% for the calibration and optimization approaches, respectively, and most are less than 0.05% and 0.005%, which means that the inverse methods themselves are reliable.

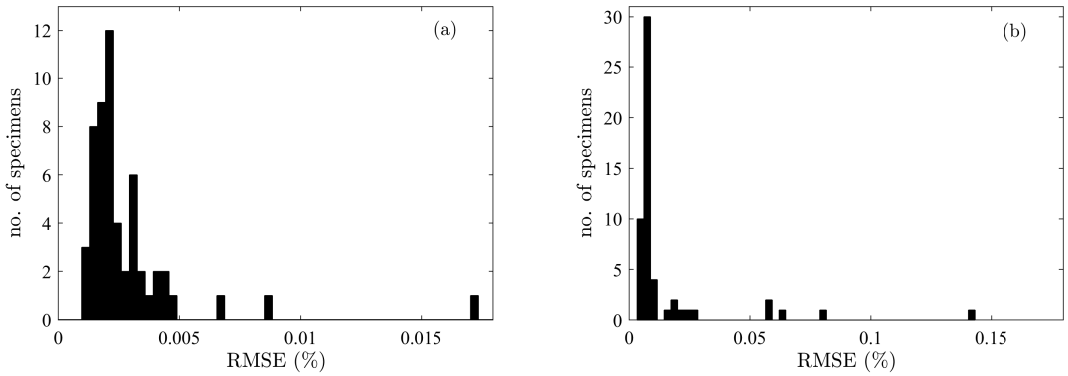

Figure C.2: Histogram of the RMSE (eq. C.1) of the specimens from the (a) optimization and (b) calibration approaches.

References

[1] J. D. Currey, Bones: structure and mechanics, Princeton university press, Princeton, 2002.

[2] Q. Grimal, K. Raum, A. Gerisch, P. Laugier, A determination of the minimum sizes of representative volume elements for the prediction of cortical bone elastic properties, Biomechanics and modeling in mechanobiology 10 (2011) 925–937.

[3] J. Y. Rho, L. Kuhn-Spearing, P. Zioupos, Mechanical properties and the hierarchical structure of bone, Medical engineering and physics 20 (1998) 92–102.

[4] A. Fritsch, C. Hellmich, 'universal' microstructural patterns in cortical and trabecular, extracellular and extravascular bone materials: Micromechanics-based prediction of anisotropic elasticity, Journal of Theoretical Biology 244 (2007) 597–620.

[5] Q. Grimal, G. Rus, W. J. Parnell, P. Laugier, A two-parameter model of the effective elastic tensor for cortical bone, Journal of biomechanics 44 (2011) 1621–1625.

[6] W. J. Parnell, M. Vu, Q. Grimal, S. Naili, Analytical methods to determine the effective mesoscopic and macroscopic elastic properties of cortical bone, Biomechanics and modeling in mechanobiology 11 (2012) 883–901.

[7] C. Hellmich, F.-J. Ulm, L. Dormieux, Can the diverse elastic properties of trabecular and cortical bone be attributed to only a few tissue-independent phase properties and their interactions?, Biomechanics and modeling in mechanobiology 2 (2004) 219–238.

[8] A. P. Baumann, J. M. Deuerling, D. J. Rudy, G. L. Niebur, R. K. Roeder, The relative influence of apatite crystal orientations and intracortical porosity on the elastic anisotropy of human cortical bone, Journal of biomechanics 45 (2012) 2743–2749.

[9] X. Cai, R. Brenner, L. Peralta, C. Olivier, P.-J. Gouttenoire, C. Chappard, F. Peyrin, D. Cassereau, P. Laugier, Q. Grimal, Homogenization of cortical bone reveals that the organization and shape of pores marginally affect elasticity, Journal of The Royal Society Interface 16 (2019) 20180911. doi:10.1098/rsif.2018.0911.

[10] H. Hemmatian, A. D. Bakker, J. Klein-Nulend, G. H. van Lenthe, Aging, osteocytes, and mechanotransduction, Current Osteoporosis Reports (2017) 1–11.

[11] M. Granke, Q. Grimal, A. Saïed, P. Nauleau, F. Peyrin, P. Laugier, Change in porosity is the major determinant of the variation of cortical bone elasticity at the millimeter scale in aged women, Bone 49 (2011) 1020–1026.

[12] C. Hoffler, K. Moore, K. Kozloff, P. Zysset, M. Brown, S. Goldstein, Heterogeneity of bone lamellar-level elastic moduli, Bone 26 (2000) 603–609.

[13] J. D. Currey, Role of collagen and other organics in the mechanical properties of bone, Osteoporosis International 14 (2003) S29–S36.

[14] B. Grabner, W. Landis, P. Roschger, S. Rinnerthaler, H. Peterlik, K. Klaushofer, P. Fratzl, Age-and genotype-dependence of bone material properties in the osteogenesis imperfecta murine model (oim), Bone 29 (2001) 453–457.

[15] Y. Bala, D. Farlay, G. Boivin, Bone mineralization: from tissue to crystal in normal and pathological contexts, Osteoporosis International 24 (2013) 2153–2166.

[16] Y. Bala, B. Depalle, D. Farlay, T. Douillard, S. Meille, H. Follet, R. Chapurlat, J. Chevalier, G. Boivin, Bone micromechanical properties are compromised during long-term alendronate therapy independently of mineralization, Journal of Bone and Mineral Research 27 (2012) 825–834.

[17] S. Ma, E. L. Goh, A. Jin, R. Bhattacharya, O. R. Boughton, B. Patel, A. Karunaratne, N. T. Vo, R. Atwood, J. P. Cobb, U. Hansen, R. L. Abel, Long-term effects of bisphosphonate therapy: perforations, microcracks and mechanical properties., Scientific reports 7 (2017) 43399.

[18] P. K. Zysset, X. Edward Guo, C. Edward Hoffler, K. E. Moore, S. A. Goldstein, Elastic modulus and hardness of cortical and trabecular bone lamellae measured by nanoindentation in the human femur, Journal of biomechanics 32 (1999) 1005–1012.

[19] G. Franzoso, P. K. Zysset, Elastic anisotropy of human cortical bone secondary osteons measured by nanoindentation, Journal of biomechanical engineering 131 (2009) 021001.

[20] K. Raum, I. Leguerney, F. Chandelier, M. Talmant, A. Saied, F. Peyrin, P. Laugier, Site-matched assessment of structural and tissue properties of cortical bone using scanning acoustic microscopy and synchrotron radiation μct, Physics in medicine and biology 51 (2006) 733.

[21] S. Yamada, S. Tadano, K. Fukasawa, Micro-cantilever bending for elastic modulus measurements of a single trabecula in cancellous bone, Journal of Biomechanics 49 (2016) 4124–4127.

[22] J. Schwiedrzik, R. Raghavan, A. Bürki, V. LeNader, U. Wolfram, J. Michler, P. Zysset, In situ micropillar compression reveals superior strength and ductility but an absence of damage in lamellar bone, Nature materials 13 (2014) 740–747.

[23] K. W. Luczynski, A. Steiger-Thirsfeld, J. Bernardi, J. Eberhardsteiner, C. Hellmich, Extracellular bone matrix exhibits hardening elastoplasticity and more than double cortical strength: evidence from homogeneous compression of non-tapered single micron-sized pillars welded to a rigid substrate, Journal of the mechanical behavior of biomedical materials 52 (2015) 51–62.

[24] C. H. Turner, J. Rho, Y. Takano, T. Y. Tsui, G. M. Pharr, The elastic properties of trabecular and cortical bone tissues are similar: results from two microscopic measurement techniques, Journal of biomechanics 32 (1999) 437–441.

[25] J.-Y. Rho, M. E. Roy, T. Y. Tsui, G. M. Pharr, Elastic properties of microstructural components of human bone tissue as measured by nanoindentation, Journal of biomedical materials research 45 (1999) 48–54.

[26] M. Granke, A. Gourrier, F. Rupin, K. Raum, F. Peyrin, M. Burghammer, A. Saïed, P. Laugier, Microfibril orientation dominates the microelastic properties of human bone tissue at the lamellar length scale, PLoS One 8 (2013) e58043.

[27] S. Schrof, P. Varga, B. Hesse, M. Schöne, R. Schütz, A. Masic, K. Raum, Multimodal correlative investigation of the interplaying micro-architecture, chemical composition and mechanical properties of human cortical bone tissue reveals predominant role of fibrillar organization in determining microelastic tissue properties, Acta Biomaterialia 44 (2016) 51–64.

[28] M. L. Oyen, R. F. Cook, A practical guide for analysis of nanoindentation data, Journal of the mechanical behavior of biomedical materials 2 (2009) 396–407.

[29] B. Preininger, S. Checa, F. L. Molnar, P. Fratzl, G. N. Duda, K. Raum, Spatial-temporal mapping of bone structural and elastic properties in a sheep model following osteotomy, Ultrasound in medicine and biology 37 (2011) 474–483.

[30] B. van Rietbergen, J. Kabel, A. Odgaard, R. Huiskes, Determination of trabecular bone tissue elastic properties by comparison of experimental and finite element results, in: Material identification using mixed numerical experimental methods, Springer, 1997, pp. 183–192.

[31] H. Daoui, X. Cai, F. Boubenider, P. Laugier, Q. Grimal, Assessment of trabecular bone tissue elasticity with resonant ultrasound spectroscopy, Journal of the mechanical behavior of biomedical materials 74 (2017) 106–110.

[32] S. Lakshmanan, A. Bodi, K. Raum, Assessment of anisotropic tissue elasticity of cortical bone from high-resolution, angular acoustic measurements, IEEE transactions on ultrasonics, ferroelectrics, and frequency control 54 (2007) 1560–1570.

[33] A. Saïed, K. Raum, I. Leguerney, P. Laugier, Spatial distribution of anisotropic acoustic impedance assessed by time-resolved 50-mhz scanning acoustic microscopy and its relation to porosity in human cortical bone., Bone 43 (2008) 187–194. doi:10.1016/j.bone.2008.02.015.

[34] U. Wolfram, H.-J. Wilke, P. K. Zysset, Transverse isotropic elastic properties of vertebral trabecular bone matrix measured using microindentation under dry conditions (effects of age, gender, and vertebral level), Journal of Mechanics in Medicine and Biology 10 (2010) 139–150.

[35] S. Bernard, Q. Grimal, P. Laugier, Accurate measurement of cortical bone elasticity tensor with resonant ultrasound spectroscopy, Journal of the mechanical behavior of biomedical materials 18 (2013) 12–19.

[36] S. Bernard, J. Schneider, P. Varga, P. Laugier, K. Raum, Q. Grimal, Elasticity-density and viscoelasticity-density relationships at the tibia mid-diaphysis assessed from resonant ultrasound spectroscopy measurements., Biomechanics and Modeling in Mechanobiology 15 (2016) 97–109.

[37] H. Moulinec, P. Suquet, A numerical method for computing the overall response of nonlinear composites with complex microstructure, Computer methods in applied mechanics and engineering 157 (1998) 69–94.

[38] R. Brenner, Numerical computation of the response of piezoelectric composites using fourier transform, Physical Review B 79 (2009) 184106.

[39] X. Cai, H. Follet, L. Peralta, M. Gardegaront, D. Farlay, R. Gauthier, B. Yu, E. Gineyts, C. Olivier, M. Langer, A. Gourrier, D. Mitton, F. Peyrin, Q. Grimal, P. Laugier, Anisotropic elastic properties of

human femoral cortical bone and relationships with composition and microstructure in elderly., Acta biomaterialia (2019). doi:10.1016/j.actbio.2019.03.043.

[40] H. S. Yoon, J. L. Katz, Ultrasonic wave propagation in human cortical bone - ii. measurements of elastic properties and microhardness, Journal of biomechanics 9 (1976) 459–464.

[41] A. A. E. Orías, J. M. Deuerling, M. D. Landrigan, J. E. Renaud, R. K. Roeder, Anatomic variation in the elastic anisotropy of cortical bone tissue in the human femur, Journal of the mechanical behavior of biomedical materials 2 (2009) 255–263.

[42] X. Cai, L. Peralta, P.-J. Gouttenoire, C. Olivier, F. Peyrin, P. Laugier, Q. Grimal, Quantification of stiffness measurement errors in resonant ultrasound spectroscopy of human cortical bone, The Journal of the Acoustical Society of America 142 (2017) 2755–2765.

[43] M. Salomé, F. Peyrin, P. Cloetens, C. Odet, A. M. Laval-Jeantet, J. Baruchel, P. Spanne, A synchrotron radiation microtomography system for the analysis of trabecular bone samples, Medical Physics 26 (1999) 2194–2204.

[44] T. Weitkamp, P. Tafforeau, E. Boller, P. Cloetens, J.-P. Valade, P. Bernard, F. Peyrin, W. Ludwig, L. Helfen, J. Baruchel, Status and evolution of the esrf beamline id19, in: X-ray Optics and Microanalysis: Proceedings of the 20th International Congress, volume 1221, 2010, pp. 33–38.

[45] S. Nuzzo, M. Lafage-Proust, E. Martin-Badosa, G. Boivin, T. Thomas, C. Alexandre, F. Peyrin, Synchrotron radiation microtomography allows the analysis of three-dimensional microarchitecture and degree of mineralization of human iliac crest biopsy specimens: Effects of etidronate treatment, Journal of Bone and Mineral Research 17 (2002) 1372–1382.

[46] J. Schindelin, I. Arganda-Carreras, E. Frise, V. Kaynig, M. Longair, T. Pietzsch, S. Preibisch, C. Rueden, S. Saalfeld, B. Schmid, et al., Fiji: an open-source platform for biological-image analysis, Nature methods 9 (2012) 676.

[47] K. Raum, I. Leguerney, F. Chandelier, E. Bossy, M. Talmant, A. Saïed, F. Peyrin, P. Laugier, Bone microstructure and elastic tissue properties are reflected in qus axial transmission measurements, Ultrasound in medicine & biology 31 (2005) 1225–1235.

[48] K. Raum, R. O. Cleveland, F. Peyrin, P. Laugier, Derivation of elastic stiffness from site-matched mineral density and acoustic impedance maps, Physics in medicine and biology 51 (2006) 747.

[49] P. Suquet, Homogenization Techniques for Composite Media (Lecture notes in Physics, vol. 272), Springer-Verlag, 1987, pp. 194–278.

[50] J. Michel, H. Moulinec, P. Suquet, Effective properties of composite materials with periodic microstructure: a computational approach, Computer methods in applied mechanics and engineering 172 (1999) 109–143.

[51] J. Swadener, G. Pharr, Indentation of elastically anisotropic half-spaces by cones and parabolae of revolution, Philosophical Magazine A 81 (2001) 447–466.

[52] S. C. Cowin, Bone mechanics handbook, CRC press, 2001.

[53] A. Migliori, J. L. Sarrao, W. M. Visscher, T. M. Bell, M. Lei, Z. Fisk, R. G. Leisure, Resonant ultrasound spectroscopic techniques for measurement of the elastic moduli of solids, Physica B 183 (1993) 1 – 24. doi:10.1016/0921-4526(93)90048-B.

[54] M. Landa, P. Sedlák, H. Seiner, L. Heller, L. Bicanová, P. Šittner, V. Novák, Modal resonant ultrasound spectroscopy for ferroelastics, Applied Physics A 96 (2009) 557–567.

[55] S. Nuzzo, F. Peyrin, P. Cloetens, J. Baruchel, G. Boivin, Quantification of the degree of mineralization of bone in three dimensions using synchrotron radiation microtomography, Medical physics 29 (2002) 2672–2681.

[56] J. Y. Rho, P. Zioupos, J. D. Currey, G. M. Pharr, Microstructural elasticity and regional heterogeneity in human femoral bone of various ages examined by nano-indentation, Journal of biomechanics 35 (2002) 189–198.

[57] T. Gross, D. H. Pahr, F. Peyrin, P. K. Zysset, Mineral heterogeneity has a minor influence on the apparent elastic properties of human cancellous bone: a srμct-based finite element study, Computer methods in biomechanics and biomedical engineering 15 (2012) 1137–1144.